

Variable thermal transport in black, blue, and violet phosphorene from extensive atomistic simulations with a neuroevolution potential

Penghua Ying,¹ Ting Liang,² Ke Xu,³ Jin Zhang,¹ Jianbin Xu,² Jianyang Wu,³ Zheyong Fan,^{4,5,*} Tapio Ala-Nissila,^{5,6} and Zheng Zhong^{1,†}

¹*School of Science, Harbin Institute of Technology, Shenzhen, 518055, P. R. China*

²*Department of Electronic Engineering and Materials Science and Technology Research Center, The Chinese University of Hong Kong, Shatin, N.T., Hong Kong SAR, 999077, P. R. China*

³*Department of Physics, Research Institute for Biomimetics and Soft Matter, Jiujiang Research Institute and Fujian Provincial Key Laboratory for Soft Functional Materials Research, Xiamen University, Xiamen 361005, PR China.*

⁴*College of Physical Science and Technology, Bohai University, Jinzhou 121013, P. R. China*

⁵*MSP group, QTF Centre of Excellence, Department of Applied Physics, Aalto University, FI-00076 Aalto, Espoo, Finland*

⁶*Interdisciplinary Centre for Mathematical Modelling, Department of Mathematical Sciences, Loughborough University, Loughborough, Leicestershire LE11 3TU, UK*

(Dated: June 17, 2022)

Phosphorus has diverse chemical bonds and even in its two-dimensional form there are three stable allotropes: black phosphorene (Black-P), blue phosphorene (Blue-P), and violet phosphorene (Violet-P). Due to the complexity of these structures, no efficient and accurate classical interatomic potential has been developed for them. In this paper, we develop an efficient machine-learned neuroevolution potential model for these allotropes and apply it to study thermal transport in them via extensive molecular dynamics (MD) simulations. Based on the homogeneous nonequilibrium MD method, the thermal conductivities are predicted to be 12.5 ± 0.2 (Black-P in armchair direction), 78.4 ± 0.4 (Black-P in zigzag direction), 128 ± 3 (Blue-P), and 2.36 ± 0.05 (Violet-P) $\text{Wm}^{-1}\text{K}^{-1}$. The underlying reasons for the significantly different thermal conductivity values in these allotropes are unraveled through spectral decomposition, phonon eigenmodes, and phonon participation ratio. Under external tensile strain, the thermal conductivity in black-P and violet-P are finite, while that in blue-P appears unbounded due to the linearization of the flexural phonon dispersion that increases the phonon mean free paths in the zero-frequency limit.

I. INTRODUCTION

Phonon thermal transport in two-dimensional (2D) materials exhibits unique properties that are absent in the bulk form [1]. After the discovery of the high thermal conductivity of graphene [2], thermal transport in other 2D materials has been actively studied. Among them, 2D phosphorene occupies a special role as there are three stable allotropes: black phosphorene (Black-P), blue phosphorene (Blue-P), and violet phosphorene (Violet-P) [3, 4]. These allotropes have very different crystalline structures: Black-P has an anisotropic orthorhombic structure with four atoms in the primitive cell (Fig. 1(a)); Blue-P has a honeycomb structure buckled perpendicular to the 2D plane with two atoms in the primitive cell (Fig. 1(b)); while Violet-P has a very complicated tubular structure with 42 atoms in the primitive cell (Fig. 1(c)). All the three allotropes are semiconductors with direct electronic bandgaps [4–6]. Therefore, phonons are the major heat carriers and phonon-dominated thermal transport in them is of great interest.

Precise measurement of the thermal conductivity κ of 2D materials is quite challenging. For Black-P, only

multi-layer samples thicker than 5 nm have been measured [8, 9] and there are so far no measurements for the other two allotropes. In this regard, computational methods play an important role in characterizing the phonon-mediated thermal transport properties in these allotropes. Boltzmann transport equation (BTE), combined with anharmonic lattice dynamics (ALD) has been the major tool for studying heat transport in various materials [10–12]. There have been quite a few BTE-ALD studies for both Black-P [13–18] and Blue-P [13, 17–20]. However, the BTE-ALD method quickly becomes computationally infeasible when the primitive cell contains a large number of atoms, which explains the absence of the application of it to Violet-P. Perhaps the most feasible method for complex crystals is based on molecular dynamics (MD) simulations which also account for phonon anharmonicity to arbitrary order and contain phonon coherence effects [21]. However, the application of MD simulation to phonon thermal transport in the phosphorene allotropes has been hindered by the lack of accurate, efficient and transferable interatomic potentials.

Recently, machine-learned potentials (MLPs) have been demonstrated to be a promising approach to enable reliable MD simulations with a reasonable computational cost [22, 23]. A Gaussian approximation potential (GAP) [24] for many phosphorus allotropes has already been developed [25] and has been shown to be

* brucenju@gmail.com

† zhongzheng@hit.edu.cn

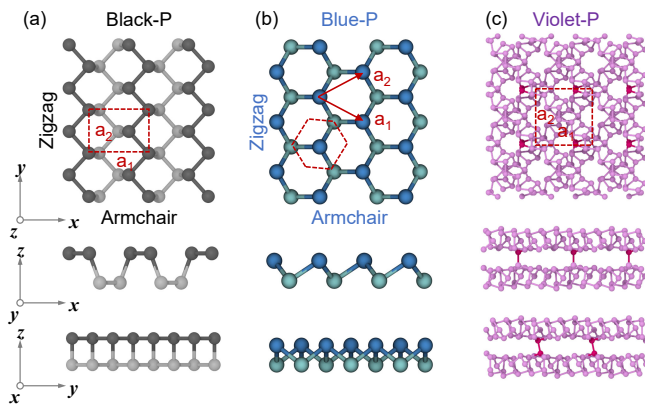


FIG. 1. Crystal structures of (a) Black-P (b) Blue-P and (c) Violet-P. The in-plane primitive cell vectors a_1 and a_2 are indicated. Black-P and Blue-P have two distinct directions that are referred to as the armchair and zigzag directions chosen to be aligned with the x and y axes, respectively. The OVITO package [7] is used for visualization.

very accurate and transferable, but the efficiency of this GAP model is currently not high enough to be used to study phonon thermal transport in the phosphorene allotropes *via* MD simulations. Another MLP framework developed by some of the present authors called the neuroevolution potential (NEP) [26–28] has been shown to have much higher computational efficiency while achieving comparable accuracy. In this paper, we use part of the training data as used for the GAP model [25] to train an accurate and highly efficient NEP model and use it to comprehensively characterize the versatile and highly varying phonon thermal transport properties of the 2D phosphorene allotropes, revealing the underlying phonon transport mechanisms and the crucial roles played by external strain in regularizing the heat transport in these materials.

II. TRAINING AND VALIDATING A NEP MODEL FOR PHOSPHORENE

NEP [26–28] is a type of MLP based on a neural network (NN) and is trained using the separable natural evolution strategy (SNES) [29]. A number of atom-environment descriptor components of a central atom are used as the input layer of the NN and the energy of the central atom is taken as the output of the NN, which is the same as in the standard Behler-Parrinello high-dimensional NN potential [30]. The site energy U_i of atom i is taken as a function of N_{des} descriptor components. To model this function, a feedforward NN with a single hidden layer with N_{neu} neurons is applied:

$$U_i = \sum_{\mu=1}^{N_{\text{neu}}} w_{\mu}^{(1)} \tanh \left(\sum_{\nu=1}^{N_{\text{des}}} w_{\mu\nu}^{(0)} q_{\nu}^i - b_{\mu}^{(0)} \right) - b^{(1)}, \quad (1)$$

where $\mathbf{w}^{(0)}$, $\mathbf{w}^{(1)}$, $\mathbf{b}^{(0)}$, and $b^{(1)}$ are the trainable weights and bias parameters in the NN and $\tanh(x)$ is the activation function.

The descriptor consists of both radial and angular components and is constructed based on Chebyshev and Legendre polynomials (or spherical harmonics via the addition theorem), inspired by previous works [30, 31]. For a central atom i , there is a set of radial descriptor components $\{q_n^i\}$ ($0 \leq n \leq n_{\text{max}}^{\text{R}}$):

$$q_n^i = \sum_{j \neq i} g_n(r_{ij}), \quad (2)$$

and a set of angular descriptor components $\{q_{nl}^i\}$ ($0 \leq n \leq n_{\text{max}}^{\text{A}}$ and $1 \leq l \leq l_{\text{max}}$):

$$q_{nl}^i = \frac{2l+1}{4\pi} \sum_{j \neq i} \sum_{k \neq i} g_n(r_{ij}) g_n(r_{ik}) P_l(\cos \theta_{ijk}). \quad (3)$$

Here the summation runs over all the neighbors of atom i within a certain cutoff distance. $P_l(\cos \theta_{ijk})$ is the Legendre polynomial of order l and θ_{ijk} is the angle formed by the ij and ik bonds.

The radial function $g_n(r_{ij})$ in Eq. 2 and Eq. 3 are defined as:

$$g_n(r_{ij}) = \frac{c_{nij}}{2} \left[T_n \left(2 \left(r_{ij}/r_c - 1 \right)^2 - 1 \right) + 1 \right] f_c(r_{ij}). \quad (4)$$

Here, $T_n(x)$ is the n^{th} order Chebyshev polynomial of the first kind and $f_c(r_{ij})$ is the cutoff function defined as

$$f_c(r_{ij}) = \begin{cases} \frac{1}{2} \left[1 + \cos \left(\pi \frac{r_{ij}}{r_c} \right) \right], & r_{ij} \leq r_c; \\ 0, & r_{ij} > r_c. \end{cases} \quad (5)$$

The cutoff radius r_c for the radial and angular descriptor components can be different, and are denoted as r_c^{R} and r_c^{A} , respectively. The coefficients c_{nij} are trainable parameters that depend on the types of the atoms i and j . The choice of the hyperparameters r_c^{R} , r_c^{A} , $n_{\text{max}}^{\text{R}}$, $n_{\text{max}}^{\text{A}}$, and l_{max} will be discussed below. The total number of descriptor components is $N_{\text{des}} = (n_{\text{max}}^{\text{R}}+1) + (n_{\text{max}}^{\text{A}}+1)l_{\text{max}}$.

The training data we used consist of the 2D phosphorene structures as constructed by Deringer *et al.* [25, 32] and 60 extra ones (20 for each of the three allotropes) with 0.1 Å random displacements for each atom starting from the equilibrium structures. For the 60 extra structures, we performed density functional theory (DFT) calculations that are consistent with those in Ref. [25], using the Perdew-Burke-Ernzerhof functional [33] plus the many-body dispersion (MBD) [34, 35], and the projector-augmented wave method [36] as implemented in VASP [37, 38]. All the calculations were converged with an energy tolerance of 10^{-8} eV under an energy cutoff of 500 eV. Finally, our training data set contains 2139 structures (51191 atoms in total) including nanoribbons, 2D structures, and bulk structures, and each structure has energy, force, and virial data. The trained NEP model

is tested against a hold-out dataset consisting of 309 2D phosphorene structures (3468 atoms in total) [39].

The NEP model was trained using the GPUMD package (version 3.3.1) [28, 40], choosing the NEP2 version. The cutoff radii for the radial and angular descriptor components are $r_c^R = 8 \text{ \AA}$ and $r_c^A = 5 \text{ \AA}$, respectively. We note that with a large radial cutoff distance of $r_c^R = 8 \text{ \AA}$, we do not need to include an empirical dispersion interaction term (such as a Lennard-Jones potential) explicitly to account for the van der Waals interactions. The Chebyshev polynomial expansion order for the radial and angular descriptor components are $n_{\max}^R = 15$ and $n_{\max}^A = 10$, respectively. The Legendre polynomial expansion order for the angular descriptor components is $l_{\max} = 4$. The number of neurons in the hidden layer of the NN is $N_{\text{neu}} = 40$.

A loss function to be minimized is defined as follows:

$$L = \lambda_1 L_1 + \lambda_2 L_2 + \lambda_e \Delta U + \lambda_f \Delta F + \lambda_v \Delta W \quad (6)$$

where ΔU , ΔF , and ΔW are the root mean square errors (RMSEs) of energy, force, and virial, respectively, between the predicted and the reference values, L_1 and L_2 are proportional to the 1-norm and 2-norm of the training parameters, and λ_e , λ_f , λ_v , λ_1 , λ_2 are the weights of the various terms. We choose $\lambda_1 = \lambda_2 = 0.05$, $\lambda_e = \lambda_f = 1$, and $\lambda_v = 0.1$. The population size and number of generations in the SNES algorithm [29] are $N_{\text{pop}} = 50$ and $N_{\text{gen}} = 2 \times 10^5$.

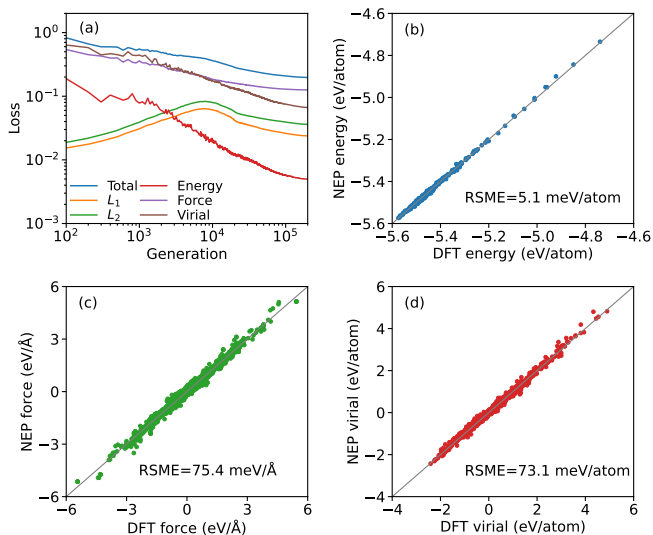


FIG. 2. (a) Evolution of various terms in the loss function for the training data set with respect to the generation in the SNES algorithm. (b) Energy, (c) force, and (d) virial calculated from NEP as compared to the reference data for the testing data set. The lines in (b)-(d) represent the identity function used to guide the eyes.

In Fig. 2(a) we show the evolution of various terms in the loss function with respect to the SNES generation during the training process. With $N_{\text{gen}} = 2 \times 10^5$

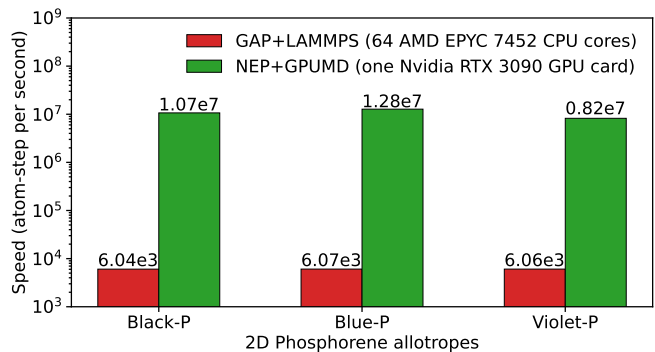


FIG. 3. A comparison of the computational speed of NEP-GPUMD (running with an Nvidia RTX 3090 GPU card) and GAP-LAMMPS (running with 64 AMD EPYC 7452 CPU cores) for the 2D phosphorene allotropes. We note that there are two versions of GAP in Ref. [25], and we used the faster one without the dispersion part to give a fair comparison with our NEP model.

generations, the RMSEs of energy, force, and virial are essentially converged. In Fig. 2 (b)-(d) we compare the energy, force, and virial predicted by the NEP model and those from DFT calculations for the testing data set. The RSMEs of energy, force, and virial are 5.1 meV/atom, 75.4 meV/Å, and 73.1 meV/atom, respectively. As a comparison, we note that the RMSEs of energy and force from GAP (virial RMSE is not available) for the 2D structures are 2.0 meV/atom and 70.0 meV/Å, respectively [25].

NEP as implemented in GPUMD attains a much higher computational performance than GAP [25] as implemented in QUIP [41] and interfaced with LAMMPS (version 14Dec2021) [42]. The computational speed is measured by running MD simulations for 100 steps in the isothermal ensemble, using 19200, 14040, and 32928 atoms for Black-P, Blue-P, and Violet-P, respectively. From Fig. 3, we see that the computational speed of NEP using a single Nvidia RTX 3090 GPU card is of the order of 10^7 atom-step per second, which is more than three orders of magnitude higher than that of GAP using 64 AMD EPYC 7452 CPU cores (two nodes, each with 32 cores). The high computational efficiency of NEP is crucial for its application to thermal transport calculations, which require extensive sampling of the phase space. To be exact, the whole MD simulations in this paper took about 1000 hours using a single Nvidia RTX 3090 GPU card.

Table I compares the lattice constants of Black-P, Blue-P, and Violet-P (see Fig. 1 for the definitions of the lattice constants) predicted by NEP with those predicted by DFT-MBD calculations. Our NEP model can predict the lattice constants of the 2D phosphorene allotropes very well, with a relative error being of the order of 0.1% in most cases and 1% for a_1 in Black-P.

The primitive cells of Black-P, Blue-P, and Violet-P

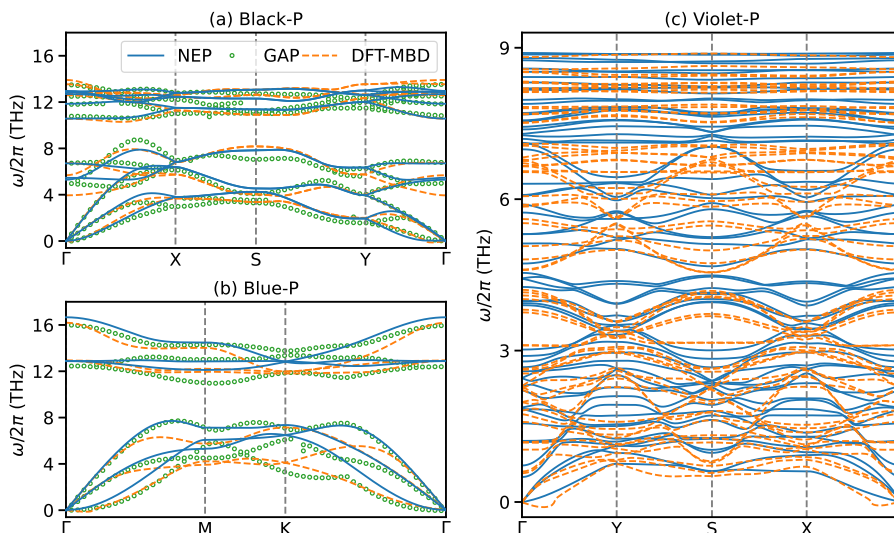


FIG. 4. Phonon dispersions of (a) Black-P, (b) Blue-P, and (c) Violet-P from the NEP model (solid lines), GAP model (circles), and DFT-MBD calculations (dashed lines). The GAP results are from Ref. [43]. Our DFT-MBD results for Black-P and Blue-P closely match those reported by Zhu *et al.* [6] and Jain *et al.* [13]. The PHONOPY package [44] is used for obtaining the DFT-MBD results.

TABLE I. A comparison between lattice constants of 2D phosphorene allotropes predicted by our NEP model and DFT-MBD calculations.

Allotrope	Black		Blue		Violet	
Lattice constant (\AA)	a_1	a_2	a_1	a_2	a_1	a_2
NEP	4.39	3.30	3.26	3.26	9.11	9.18
DFT-MBD	4.33	3.31	3.26	3.26	9.12	9.18

are 4, 2, and 42, respectively, leading to 12, 6, and 126 phonon branches, respectively. Despite the very different phonon dispersions, our NEP model can well describe them simultaneously, exhibiting a level of accuracy similar to the GAP model, as can be seen from Fig. 4. This is beyond the reach of any current empirical potential. For Blue-P, the frequencies around the M and K points are overestimated as compared to DFT-MBD, but those around the Γ point are well described. The complex phonon dispersions of Violet-P are also reasonably described by NEP, which even behaves more nicely around the Γ point than DFT-MBD which suffers from some numerical issues.

We note that there is a phonon band gap with 2.6 THz (7.9 to 10.5 THz) in Black-P and one with 4.6 THz (7.7 to 12.3 THz) in Blue-P, while there is no evident gap in Violet-P. In the case of Violet-P which has a large unit cell, there are flat bands at lower frequencies, and significant overlap between multiple bands in which case approaches based on the linearized BTE are expected to fail [45]. Based on the band picture we expect a high degree of phonon localization in Violet-P that should lead to a low value of thermal conductivity.

Before detailed calculations, we can also infer some interesting properties based on the acoustic branches. In Black-P, the acoustic branches are much higher in the Γ -X (zigzag) direction than in the Γ -Y (armchair) direction, leading to higher group velocities in the zigzag direction, which is one of the origins of the highly anisotropic phonon transport in Black-P. In the other two allotropes, there is no such anisotropy. As mentioned above, the acoustic branches of Violet-P are much flatter than the other two allotropes, leading to much lower phonon group velocities. This is also related to the flexibility of Violet-P under deformation, which is caused by a unique deformation mode, namely, rotation of sub-nano rods [46].

III. PHONON THERMAL TRANSPORT IN PHOSPHORENE ALLOTROPES

For a quantitative study we computed the thermal conductivity using the homogeneous non-equilibrium molecular dynamics (HNEMD) method [47, 48] which has been shown to be an efficient approach in various 2D materials [49–56]. In this method, an external force is applied to each atom i to drive the system out of equilibrium. The external force $\mathbf{F}_i^{\text{ext}}$ can be written in terms of the per-atom energy E_i and virial tensor \mathbf{W}_i as follows [57]:

$$\mathbf{F}_i^{\text{ext}} = E_i \mathbf{F}_e + \mathbf{F}_e \cdot \mathbf{W}_i, \quad (7)$$

where \mathbf{F}_e is the driving force parameter with the dimension of inverse length. The driving force will induce a nonequilibrium heat current $J(t)$ as a function of time t

that is linearly proportional to $F_e = |\mathbf{F}_e|$,

$$\kappa(t) = \frac{J(t)}{TVF_e}, \quad (8)$$

where $\kappa(t)$ is the instant thermal conductivity, V is the volume, and T is the temperature. In the calculation of V , the thicknesses of Black-P [58], Blue-P [6], and Violet-P [4] are respectively taken as 5.25 Å, 5.63 Å, and 11.00 Å. The temperature needs to be maintained by using a thermostat, and to this end, we use the Nosé-Hoover chain thermostat with a relaxation time of 100 fs. In all our MD simulations, a time step of 1 fs is used. The in-plane simulation cell size is set to 25 nm × 25 nm which is sufficiently large based on our tests.

To check the convergence of $\kappa(t)$, it is conventional to redefine the thermal conductivity as [48]:

$$\kappa(t) = \frac{1}{t} \int_0^t \frac{J(\tau)}{TVF_e} d\tau. \quad (9)$$

The magnitude of the driving force parameter F_e should be small enough to keep the system within the linear response regime and large enough to keep a reasonably large signal-to-noise ratio. An upper bound of $F_e = 1/\lambda_{\max}$ has been suggested [48], where λ_{\max} is the maximum phonon mean free path in the system, as will be further confirmed below.

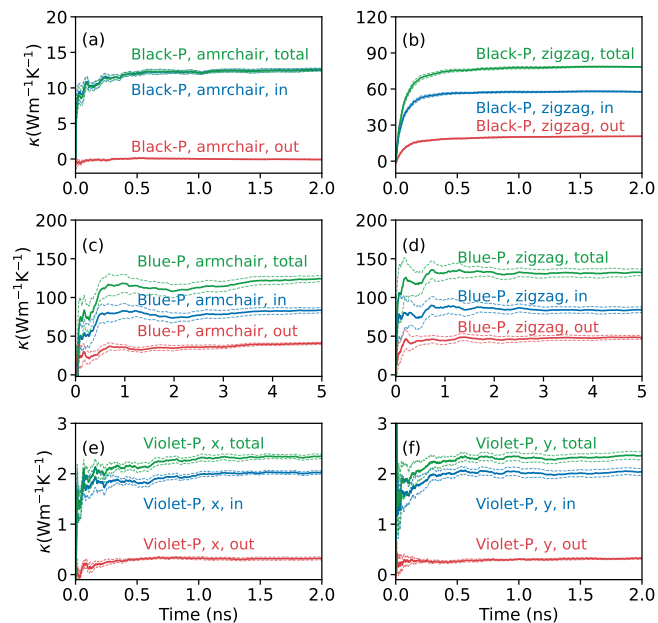


FIG. 5. (a)-(f) The thermal conductivity as defined in Eq. 9 for the phosphorene allotropes at 300 K and zero pressure, along the zigzag/armchair or x/y directions as defined in Fig. 1. In each subplot, the total thermal conductivity (“total”) is decomposed into contributions from in-plane (“in”) and out-of-plane (“out”) phonon modes. Solid lines are averaged values and dashed ones represent the error bounds from ten independent runs.

For the $\kappa(t)$ obtained by using Eq. 9 in HNEMD simulations, we set $F_e = 0.1 \mu\text{m}^{-1}$ for Blue-P (Fig. 5(c)-(d)) and $F_e = 1.0 \mu\text{m}^{-1}$ for Black-P (Fig. 5(a)-(b)) and Violet-P (Fig. 5(e)-(f)). We performed ten independent runs, each with a 100 ps equilibration stage in the isothermal-isobaric ensemble (with a target in-plane pressure of zero and a target temperature of 300 K), and after that, a 2-ns production stage for black and Violet-P, or a 5-ns production stage for Blue-P.

In Fig. 5, we decompose [48] κ into contributions from in-plane (κ_{in}) and out-of-plane (flexural) (κ_{out}) phonon modes, $\kappa = \kappa_{\text{in}} + \kappa_{\text{out}}$. For all the allotropes, κ_{in} dominates, which means that flexural phonons are not the major heat carrier in phosphorene. Among the three allotropes, Blue-P has the highest thermal conductivity $128 \pm 3 \text{ Wm}^{-1}\text{K}^{-1}$, which is about two orders of magnitude higher than that in Violet-P ($2.36 \pm 0.05 \text{ Wm}^{-1}\text{K}^{-1}$). While these two allotropes are isotropic for in-plane heat transport, Black-P exhibits strong anisotropy, with κ in the zigzag direction ($78.4 \pm 0.4 \text{ Wm}^{-1}\text{K}^{-1}$) being about six times as large as that in the armchair direction ($12.5 \pm 0.2 \text{ Wm}^{-1}\text{K}^{-1}$). Both the strong anisotropy and the magnitudes of the thermal conductivity in Black-P and Blue-P are well consistent with the existing BTE-ALD predictions based on DFT-based force constants [14–20]. While the simultaneous description of two or more distinct structures is generally beyond the capability of empirical potentials, the results here suggest that our NEP model has this capability. For the most complex allotrope, Violet-P, the BTE-ALD approach is computationally infeasible and we thus have a prediction for its thermal conductivity for the first time. As suggested by the phonon band picture, its magnitude is among the smallest found for elementary crystals.

To get more insight in the physical mechanisms behind the highly variable phonon transport in 2D phosphorene, we used the spectral decomposition techniques in Refs. 48 and 57 to calculate the diffusive spectral thermal conductivity $\kappa(\omega)$ and the ballistic spectral thermal conductance $G(\omega)$, as shown in Fig. 6(a) and Fig. 6(b), respectively. From $\kappa(\omega)$ and $G(\omega)$, one can readily calculate the frequency-dependent phonon mean free path (MFP) [48]:

$$\lambda(\omega) = \kappa(\omega)/G(\omega), \quad (10)$$

as shown in Fig. 6(c). Then, one can obtain the thermal conductivity at any length L [48],

$$\kappa(L) = \int_0^\infty \frac{d\omega}{2\pi} \frac{\kappa(\omega)L}{L + \lambda(\omega)}, \quad (11)$$

as shown in Fig. 6(d).

The phonon band gaps in Fig. 4 are also manifested in the spectral quantities here. For all the allotropes, κ gets its main contribution from the acoustic phonon branches. The maximum phonon MFP λ_{\max} in all the allotropes is located at the low-frequency limit, reaching about 10^4 nm in Blue-P, 10^3 nm in the zigzag direction

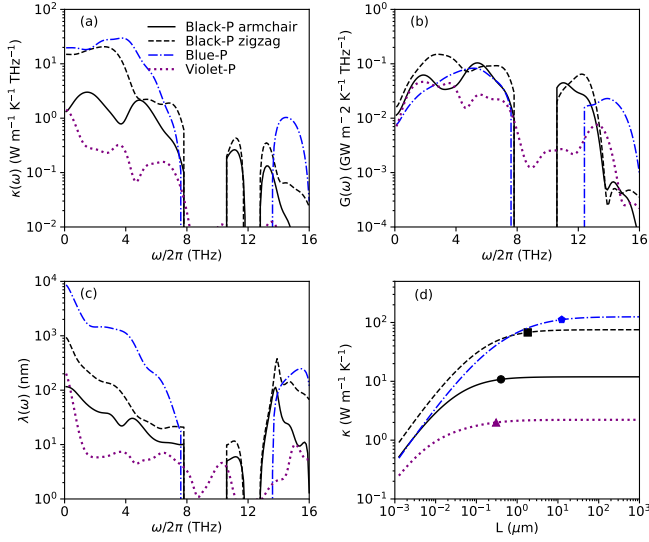


FIG. 6. (a) Diffusive spectral thermal conductivity $\kappa(\omega)$, (b) ballistic spectral thermal conductance $G(\omega)$, (c) phonon mean free path $\lambda(\omega)$, and (d) length-dependent thermal conductivity $\kappa(L)$ for the phosphorene allotropes at 300 K and zero pressure. The symbols in (d) denote the system lengths needed to reach 90% of the convergent κ for each allotrope.

of Black-P, and 10² nm in Violet-P and the armchair direction of Black-P. These results are well consistent with our choice of the driving force parameter F_e that ensures $F_e \lambda_{\max} \lesssim 1$. Consistent with the different MFPs, the allotropes exhibit different convergence rates of $\kappa(L)$ with increasing L . It requires more than 10 microns to reach 90% of the diffusive κ in Blue-P, while only requires a few hundred nanometers to reach 90% of the diffusive κ in Violet-P.

From Fig. 6(c), we see that the phonon MFPs in Violet-P are smaller than 10 nm for $\omega/2\pi \gtrsim 1$ THz. This indicates that most of the phonon modes in Violet-P are localized, which can be confirmed by the optical phonon eigenmodes at the Γ point shown in Fig. 7, obtained using the method in Ref. 59. In both Black-P and Blue-P, the optical eigenmodes at relatively high frequencies exhibit collective movements of the atoms. In contrast, the optical eigenmodes in Violet-P only show collective behavior below 1 THz, and random movements of the atoms starting from 1.2 THz. This indicates that the phonon modes in Violet-P are well localized for $\omega/2\pi \gtrsim 1$ THz.

Phonon localization can be quantified by the phonon participation ratios (PPR) [60] defined as

$$R(\omega) = \frac{1}{N} \frac{(\sum_i \rho_i^2(\omega))^2}{\sum_i \rho_i^4(\omega)}, \quad (12)$$

where $\rho_i(\omega)$ is the phonon density of states of atom i and N is the total number of atoms involved in the calculation. A value of $R = 1$ represents a totally de-localized mode, and a smaller value corresponds to a stronger lo-

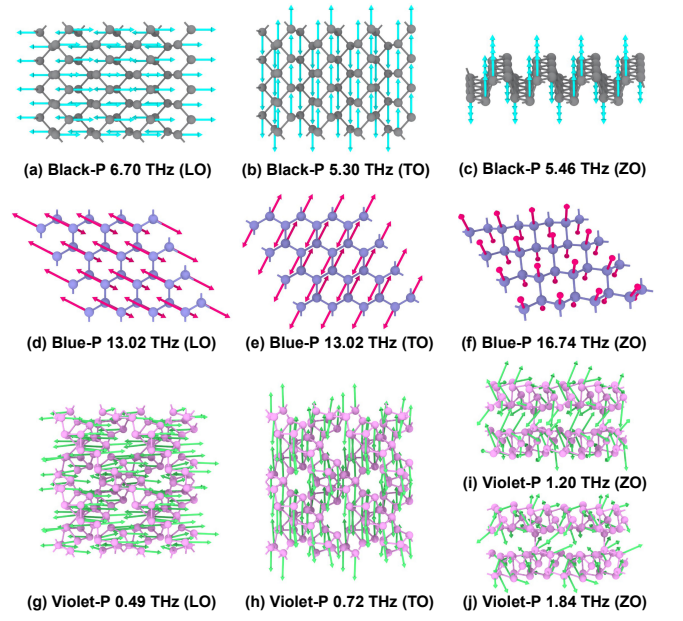


FIG. 7. Phonon eigenmodes for (a)-(c) Black-P, (d)-(f) Blue-P, and (g)-(j) Violet-P at selected frequencies $\omega/2\pi$ at the Γ point. The magnitude and direction of an arrow represent the eigenvector component at an atom. LO, TO, and ZO represent the longitudinal, transverse, and out-of-plane optical phonon modes, respectively. The OVITO package [7] is used for visualization.

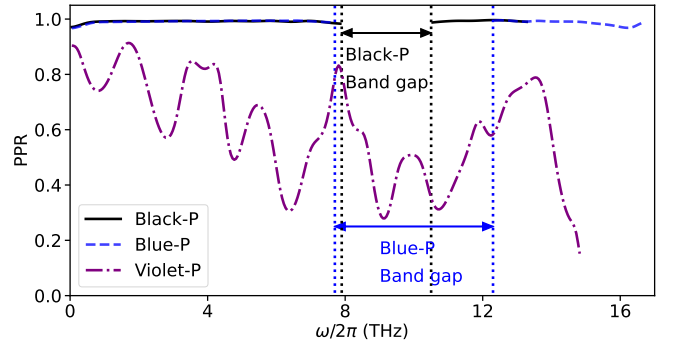


FIG. 8. Phonon participation ratio as a function of phonon frequency for Black-P, Blue-P, and Violet-P at 300 K and zero pressure.

calization. Fig. 8 shows that the phonon modes in Black-P and Blue-P are essentially de-localized up to the maximum frequency, while those in Violet-P are strongly localized and its PPR generally decreases with increasing phonon frequency. The strong localization of phonons in Violet-P is consistent with the relatively flat phonon bands and the low phonon group velocities (Fig. 4(c)).

In Fig. 9 we show the temperature-dependent κ for the three phosphorene allotropes. Black-P and Blue-P largely follow a typical T^{-1} dependence of κ as domi-

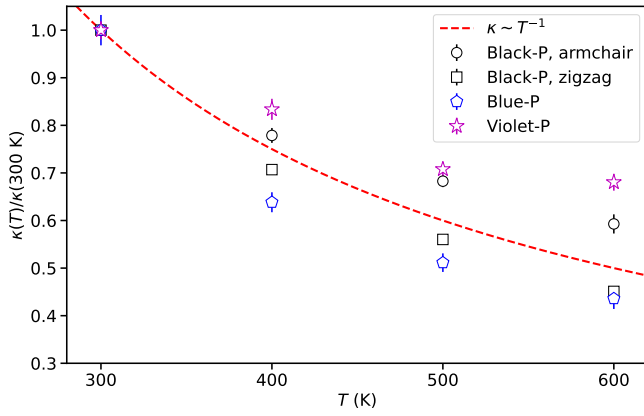


FIG. 9. Thermal conductivity κ for the phosphorene allotropes as a function of temperature T . For each allotrope, κ is normalized by its value at 300 K.

nated by three-phonon scattering processes. However, Violet-P exhibits a clearly weaker temperature dependence, $\kappa \sim T^{-0.59}$, which suggests the importance of high-order anharmonicity as in low- κ materials [61, 62]

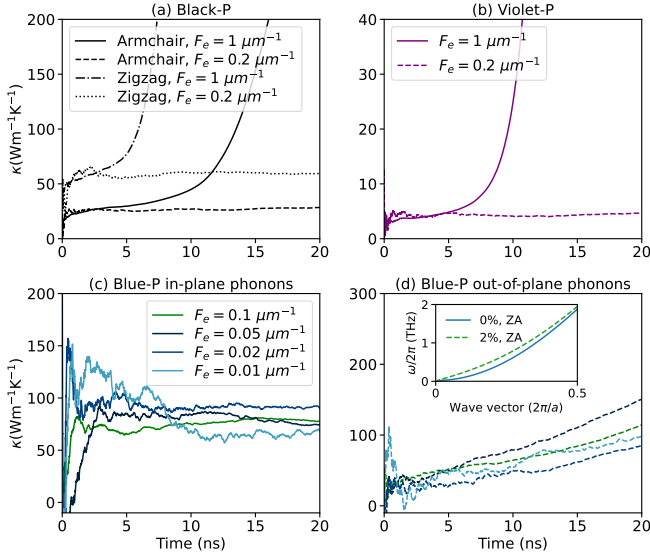


FIG. 10. The thermal conductivity as defined in Eq. 9 for the phosphorene allotropes at 300 K and different in-plane strain levels: (a) Black-P under 4% uniaxial tensile strain, (b) Violet-P, (c)-(d) Blue-P under 2% biaxial tensile strain. The inset in (d) shows the change of the ZA branch of Blue-P along the Γ -M path upon the application of 2% bi-axial tensile strain.

An interesting observation in graphene [63, 64] and graphene-like 2D materials [65–69] is that the thermal conductivity might be not upper bounded or increase significantly under external strain. Here we use the HNEMD method to examine this issue for the phospho-

rene allotropes. For Black-P, we apply a 4% uniaxial tensile strain in the armchair or zigzag direction. For Blue-P and Violet-P, we apply 2% biaxial tensile strain. Our argument below relies on the criteria of $F_e \lambda_{\max} \lesssim 1$ for keeping the system within the linear-response regime in the HNEMD simulations. In this case, the $\kappa(t)$ defined in Eq. 9 should converge in the long-time limit. In all the cases we perform HNEMD simulations up to a long time of 20 ns, which is needed to clearly identify possible $\kappa(t)$ divergence.

The $\kappa(t)$ as defined in Eq. 9 in the strained systems are shown in Fig. 10. For Black-P and Violet-P, using the value $F_e = 1 \mu\text{m}^{-1}$ as adopted in the unstrained condition leads to divergent $\kappa(t)$, but the convergence of $\kappa(t)$ can be restored by reducing F_e to $0.2 \mu\text{m}^{-1}$. This means that λ_{\max} increases in Black-P and Violet-P under the external strain but is still finite and κ is thus still finite.

The situation is notably different in Blue-P, which exhibits divergent $\kappa(t)$ even if F_e is reduced from 0.1 to 0.01 μm^{-1} . This means that λ_{\max} in 2% bi-axially stretched Blue-P is at least 100 μm , which in turn means that $\kappa(L)$ does not converge before the millimeter length scale. We cannot indefinitely reduce F_e to probe a possible upper bound of λ_{\max} because of the reduced signal-to-noise ratio with decreased F_e in the HNEMD simulations. Nevertheless, our results here do not show a sign of convergence trend of $\kappa(t)$ and we conclude that the thermal conductivity in 2% bi-axially stretched Blue-P appears unbounded.

The out-of-plane phonons are responsible for the increased λ_{\max} under stretching (Fig. 10(d)). This is in turn related to the linearization of the ZA phonon dispersion around the Γ point as shown in the inset of Fig. 10(d). Indeed, in the case of silicene, a buckled 2D material similar to Blue-P, a linear dispersion of the ZA branch can lead to divergent κ even in the unstrained condition, according to the BTE-ALD approach [1, 70]. Our findings for strained Blue-P here are consistent with previous BTE-ALD results [65–69] on strained graphene-like materials, although only three-phonon scattering processes were considered in the BTE-ALD approach. Our MD simulations demonstrate the diverse effects of external strain on the thermal conductivity of general 2D materials in the non-perturbative regime.

IV. SUMMARY AND CONCLUSIONS

In summary, we have constructed a unified MLP for three 2D phosphorene allotropes, Black-P, Blue-P, and Violet-P, based on the NEP model [26–28] that has a comparable accuracy to the existing GAP model [25] and a far superior computational efficiency. With this NEP model, we performed large-scale MD simulations to study thermal transport in these phosphorene allotropes. For Black-P and Blue-P, our predicted thermal conductivity based on HNEMD simulations are consistent with liter-

ature results based on the BTE-ALD approach, and for Violet-P, our approach allowed for the prediction of its thermal conductivity for the first time. We found that Violet-P has a much smaller thermal conductivity than Black-P and Blue-P, due to the strong phonon localization in this material. Finally, we find that, under external tensile strain, the thermal conductivity in Black-P and Violet-P are still finite, but that in Blue-P is still not convergent at least up to the millimeter length scale, due to the linearization of the flexural phonon dispersion.

Data availability:

Complete input and output files for the NEP training and testing are freely available at a Zenodo repository [71].

ACKNOWLEDGMENTS

We thank Xin Wu, Yanzhou Wang, and Zezhu Zeng for insightful discussions. P.Y. and Z.Z. acknowledge the supports from the National Key R&D Program of China (No. 2018YFB1502602) and the National Natural Science Foundation of China (Nos. 11932005 and 11772106). T.L. and J.X. acknowledge the support from the Research Grants Council of Hong Kong (Grant No. AoE/P-02/12). Z.F. acknowledges support from the National Natural Science Foundation of China (No. 11974059). T.A-N. has been supported in part by the Academy of Finland through its QTF Centre of Excellence program (No. 312298) and Technology Industries of Finland Centennial Foundation Future Makers grant.

-
- [1] X. Gu, Y. Wei, X. Yin, B. Li, and R. Yang, Colloquium: Phononic thermal properties of two-dimensional materials, *Rev. Mod. Phys.* **90**, 041002 (2018).
- [2] A. A. Balandin, S. Ghosh, W. Bao, I. Calizo, D. Teweldebrhan, F. Miao, and C. N. Lau, Superior thermal conductivity of single-layer graphene, *Nano Letters* **8**, 902 (2008).
- [3] A. Carvalho, M. Wang, X. Zhu, A. S. Rodin, H. Su, and A. H. Castro Neto, Phosphorene: from theory to applications, *Nature Reviews Materials* **1**, 1 (2016).
- [4] L. Zhang, H. Huang, B. Zhang, M. Gu, D. Zhao, X. Zhao, L. Li, J. Zhou, K. Wu, Y. Cheng, *et al.*, Structure and properties of violet phosphorus and its phosphorene exfoliation, *Angewandte Chemie International Edition* **59**, 1074 (2020).
- [5] V. Tran, R. Soklaski, Y. Liang, and L. Yang, Layer-controlled band gap and anisotropic excitons in few-layer black phosphorus, *Physical Review B* **89**, 235319 (2014).
- [6] Z. Zhu and D. Tománek, Semiconducting layered blue phosphorus: a computational study, *Physical Review Letters* **112**, 176802 (2014).
- [7] A. Stukowski, Visualization and analysis of atomistic simulation data with OVITO—the Open Visualization Tool, *Modelling and Simulation in Materials Science and Engineering* **18**, 015012 (2009).
- [8] H. Jang, J. D. Wood, C. R. Ryder, M. C. Hersam, and D. G. Cahill, Anisotropic Thermal Conductivity of Exfoliated Black Phosphorus, *Advanced Materials* **27**, 8017 (2015).
- [9] Z. Luo, J. Maassen, Y. Deng, Y. Du, R. P. Garrelts, M. S. Lundstrom, P. D. Ye, and X. Xu, Anisotropic in-plane thermal conductivity observed in few-layer black phosphorus, *Nature Communications* **6**, 1 (2015).
- [10] L. Lindsay, First principles Peierls-Boltzmann phonon thermal transport: a topical review, *Nanoscale and Microscale Thermophysical Engineering* **20**, 67 (2016).
- [11] A. J. McGaughey, A. Jain, H.-Y. Kim, and B. Fu, Phonon properties and thermal conductivity from first principles, lattice dynamics, and the Boltzmann transport equation, *Journal of Applied Physics* **125**, 011101 (2019).
- [12] H. Bao, J. Chen, X. Gu, and B. Cao, A Review of Simulation Methods in Micro/Nanoscale Heat Conduction, *ES Energy & Environment* **1**, 16 (2018).
- [13] A. Jain and A. J. McGaughey, Strongly anisotropic in-plane thermal transport in single-layer black phosphorene, *Scientific Reports* **5**, 1 (2015).
- [14] L. Zhu, G. Zhang, and B. Li, Coexistence of size-dependent and size-independent thermal conductivities in phosphorene, *Physical Review B* **90**, 214302 (2014).
- [15] G. Qin, Q.-B. Yan, Z. Qin, S.-Y. Yue, M. Hu, and G. Su, Anisotropic intrinsic lattice thermal conductivity of phosphorene from first principles, *Physical Chemistry Chemical Physics* **17**, 4854 (2015).
- [16] T.-H. Liu and C.-C. Chang, Anisotropic thermal transport in phosphorene: effects of crystal orientation, *Nanoscale* **7**, 10648 (2015).
- [17] G. Zheng, Y. Jia, S. Gao, and S.-H. Ke, Comparative study of thermal properties of group-VA monolayers with buckled and puckered honeycomb structures, *Physical Review B* **94**, 155448 (2016).
- [18] J. Zhang, H. Liu, L. Cheng, J. Wei, J. Liang, D. Fan, P. Jiang, and J. Shi, Thermal conductivities of phosphorene allotropes from first-principles calculations: a comparative study, *Scientific Reports* **7**, 1 (2017).
- [19] Z. Liu, J. Morales-Ferreiro, and T. Luo, First-principles study of thermoelectric properties of blue phosphorene, *Applied Physics Letters* **113**, 063903 (2018).
- [20] H. Zhu, No-monotonic strain effect on the thermal conductivity of blue phosphorene: A first-principles study, *Physica E: Low-dimensional Systems and Nanostructures* **124**, 114341 (2020).
- [21] Z. Zhang, Y. Guo, M. Bescond, J. Chen, M. Nomura, and S. Volz, Heat conduction theory including phonon coherence, *Physical Review Letters* **128**, 015901 (2022).
- [22] J. Behler, Perspective: Machine learning potentials for atomistic simulations, *The Journal of chemical physics* **145**, 170901 (2016).
- [23] V. L. Deringer, M. A. Caro, and G. Csányi, Machine learning interatomic potentials as emerging tools for materials science, *Advanced Materials* **31**, 1902765 (2019).
- [24] A. P. Bartók, M. C. Payne, R. Kondor, and G. Csányi, Gaussian approximation potentials: The accuracy of quantum mechanics, without the electrons, *Physical Review Letters* **104**, 136403 (2010).
- [25] V. L. Deringer, M. A. Caro, and G. Csányi, A general-purpose machine-learning force field for bulk and nanos-

- structured phosphorus, *Nature Communications* **11**, 1 (2020).
- [26] Z. Fan, Z. Zeng, C. Zhang, Y. Wang, K. Song, H. Dong, Y. Chen, and T. Ala-Nissila, Neuroevolution machine learning potentials: Combining high accuracy and low cost in atomistic simulations and application to heat transport, *Physical Review B* **104**, 104309 (2021).
- [27] Z. Fan, Improving the accuracy of the neuroevolution machine learning potential for multi-component systems, *Journal of Physics: Condensed Matter* **34**, 125902 (2022).
- [28] Z. Fan, Y. Wang, P. Ying, K. Song, J. Wang, Y. Wang, Z. Zeng, K. Xu, E. Lindgren, J. M. Rahm, A. J. Gabourie, J. Liu, H. Dong, J. Wu, Y. Chen, Z. Zhong, J. Sun, P. Erhart, Y. Su, and T. Ala-Nissila, GPUMD: A package for constructing accurate machine-learned potentials and performing highly efficient atomistic simulations (2022), [arXiv:2205.10046 \[physics.comp-ph\]](https://arxiv.org/abs/2205.10046).
- [29] T. Schaul, T. Glasmachers, and J. Schmidhuber, High Dimensions and Heavy Tails for Natural Evolution Strategies, in *Proceedings of the 13th Annual Conference on Genetic and Evolutionary Computation*, GECCO '11 (Association for Computing Machinery, New York, NY, USA, 2011) pp. 845–852.
- [30] J. Behler and M. Parrinello, Generalized neural-network representation of high-dimensional potential-energy surfaces, *Physical Review Letters* **98**, 146401 (2007).
- [31] M. A. Caro, Optimizing many-body atomic descriptors for enhanced computational performance of machine learning based interatomic potentials, *Physical Review B* **100**, 024112 (2019).
- [32] V. L. Deringer, M. A. Caro, and G. Csányi, *GAP-20 machine learning force field for phosphorus* (2020).
- [33] J. P. Perdew, K. Burke, and M. Ernzerhof, Generalized gradient approximation made simple, *Physical Review Letters* **77**, 3865 (1996).
- [34] A. Tkatchenko, R. A. DiStasio Jr, R. Car, and M. Scheffler, Accurate and efficient method for many-body van der Waals interactions, *Physical Review Letters* **108**, 236402 (2012).
- [35] A. Ambrosetti, A. M. Reilly, R. A. DiStasio Jr, and A. Tkatchenko, Long-range correlation energy calculated from coupled atomic response functions, *The Journal of Chemical Physics* **140**, 18A508 (2014).
- [36] P. E. Blöchl, Projector augmented-wave method, *Physical Review B* **50**, 17953 (1994).
- [37] G. Kresse and J. Furthmüller, Efficient iterative schemes for ab initio total-energy calculations using a plane-wave basis set, *Physical Review B* **54**, 11169 (1996).
- [38] G. Kresse and D. Joubert, From ultrasoft pseudopotentials to the projector augmented-wave method, *Physical Review B* **59**, 1758 (1999).
- [39] <https://github.com/libAtoms/testing-framework/tree/public/tests/P>.
- [40] Z. Fan, W. Chen, V. Vierimaa, and A. Harju, Efficient molecular dynamics simulations with many-body potentials on graphics processing units, *Computer Physics Communications* **218**, 10 (2017).
- [41] <https://github.com/libAtoms/QUIP>.
- [42] A. P. Thompson, H. M. Aktulga, R. Berger, D. S. Bolintineanu, W. M. Brown, P. S. Crozier, P. J. in't Veld, A. Kohlmeyer, S. G. Moore, T. D. Nguyen, *et al.*, LAMMPS—a flexible simulation tool for particle-based materials modeling at the atomic, meso, and continuum scales, *Computer Physics Communications* **271**, 108171 (2022).
- [43] A. Koneru, R. Batra, S. Manna, T. D. Loeffler, H. Chan, M. Sternberg, A. Avarca, H. Singh, M. J. Cherukara, and S. K. Sankaranarayanan, Multi-reward Reinforcement Learning Based Bond-Order Potential to Study Strain-Assisted Phase Transitions in Phosphorene, *The Journal of Physical Chemistry Letters* **13**, 1886 (2022).
- [44] A. Togo and I. Tanaka, First principles phonon calculations in materials science, *Scripta Materialia* **108**, 1 (2015).
- [45] M. Simoncelli, N. Marzari, and F. Mauri, Unified theory of thermal transport in crystals and glasses, *Nature Physics* **15**, 809 (2019).
- [46] P. Ying, X. Li, X. Qiang, Y. Du, J. Zhang, L. Chen, and Z. Zhong, Tension-Induced Phase Transformation and Anomalous Poisson Effect in Violet Phosphorene, *ChemRxiv* [10.26434/chemrxiv-2022-kw6tp](https://doi.org/10.26434/chemrxiv-2022-kw6tp) (2022).
- [47] D. J. Evans, Homogeneous NEMD algorithm for thermal conductivity—application of non-canonical linear response theory, *Physics Letters A* **91**, 457 (1982).
- [48] Z. Fan, H. Dong, A. Harju, and T. Ala-Nissila, Homogeneous nonequilibrium molecular dynamics method for heat transport and spectral decomposition with many-body potentials, *Physical Review B* **99**, 064308 (2019).
- [49] H. Dong, P. Hirvonen, Z. Fan, and T. Ala-Nissila, Heat transport in pristine and polycrystalline single-layer hexagonal boron nitride, *Physical Chemistry Chemical Physics* **20**, 24602 (2018).
- [50] K. Xu, Z. Fan, J. Zhang, N. Wei, and T. Ala-Nissila, Thermal transport properties of single-layer black phosphorus from extensive molecular dynamics simulations, *Modelling and Simulation in Materials Science and Engineering* **26**, 085001 (2018).
- [51] A. J. Gabourie, S. V. Suryavanshi, A. B. Farimani, and E. Pop, Reduced thermal conductivity of supported and encased monolayer and bilayer MoS₂, *2D Materials* **8**, 011001 (2020).
- [52] X. Wu and Q. Han, Thermal transport in pristine and defective two-dimensional polyaniline (C₃N), *International Journal of Heat and Mass Transfer* **173**, 121235 (2021).
- [53] S. E. Kim, F. Mujid, A. Rai, F. Eriksson, J. Suh, P. Poddar, A. Ray, C. Park, E. Fransson, Y. Zhong, *et al.*, Extremely anisotropic van der Waals thermal conductors, *Nature* **597**, 660 (2021).
- [54] H. Wang, Y. Cheng, Z. Fan, Y. Guo, Z. Zhang, M. Bescond, M. Nomura, T. Ala-Nissila, S. Volz, and S. Xiong, Anomalous thermal conductivity enhancement in low dimensional resonant nanostructures due to imperfections, *Nanoscale* **13**, 10010 (2021).
- [55] P. Ying, T. Liang, Y. Du, J. Zhang, X. Zeng, and Z. Zhong, Thermal transport in planar sp²-hybridized carbon allotropes: A comparative study of biphenylene network, pentaheptite and graphene, *International Journal of Heat and Mass Transfer* **183**, 122060 (2022).
- [56] W. Sha and F. Guo, Thermal transport in two-dimensional carbon nitrides: A comparative molecular dynamics study, *Carbon Trends* **7**, 100161 (2022).
- [57] A. J. Gabourie, Z. Fan, T. Ala-Nissila, and E. Pop, Spectral decomposition of thermal conductivity: Comparing velocity decomposition methods in homogeneous molecular dynamics simulations, *Physical Review B* **103**, 205421 (2021).
- [58] T. Akai, S. Endo, Y. Akahama, K. Koto, and Y. Maruyama, The crystal structure and oriented trans-

- formation of black phosphorus under high pressure, *International Journal of High Pressure Research* **1**, 115 (1989).
- [59] T. Liang, K. Xu, M. Han, Y. Yao, Z. Zhang, X. Zeng, J. Xu, and J. Wu, Abnormally high thermal conductivity in fivefold twinned diamond nanowires, *Materials Today Physics* **25**, 100705 (2022).
- [60] S. Burkov, B. Koltenbah, and L. Bruch, Phonon localization in one-dimensional quasiperiodic chains, *Physical Review B* **53**, 14179 (1996).
- [61] Z. Zeng, C. Zhang, H. Yu, W. Li, Y. Pei, and Y. Chen, Ultralow and glass-like lattice thermal conductivity in crystalline BaAg₂Te₂: Strong fourth-order anharmonicity and crucial diffusive thermal transport, *Materials Today Physics* **21**, 100487 (2021).
- [62] Z. Zeng, C. Chen, C. Zhang, Q. Zhang, and Y. Chen, Critical phonon frequency renormalization and dual phonon coexistence in layered Ruddlesden-Popper inorganic perovskites, *Physical Review B* **105**, 184303 (2022).
- [63] L. F. C. Pereira and D. Donadio, Divergence of the thermal conductivity in uniaxially strained graphene, *Phys. Rev. B* **87**, 125424 (2013).
- [64] Z. Fan, L. F. C. Pereira, P. Hirvonen, M. M. Ervasti, K. R. Elder, D. Donadio, T. Ala-Nissila, and A. Harju, Thermal conductivity decomposition in two-dimensional materials: Application to graphene, *Physical Review B* **95**, 144309 (2017).
- [65] Y. Kuang, L. Lindsay, S. Shi, and G. Zheng, Tensile strains give rise to strong size effects for thermal conductivities of silicene, germanene and stanene, *Nanoscale* **8**, 3760 (2016).
- [66] H. Xie, T. Ouyang, É. Germaneau, G. Qin, M. Hu, and H. Bao, Large tunability of lattice thermal conductivity of monolayer silicene via mechanical strain, *Physical Review B* **93**, 075404 (2016).
- [67] S. Li and Y. Chen, Thermal transport and anharmonic phonons in strained monolayer hexagonal boron nitride, *Scientific Reports* **7**, 1 (2017).
- [68] M. Raeisi, S. Ahmadi, and A. Rajabpour, Modulated thermal conductivity of 2D hexagonal boron arsenide: a strain engineering study, *Nanoscale* **11**, 21799 (2019).
- [69] A. Banerjee, B. K. Das, and K. K. Chattopadhyay, Significant enhancement of lattice thermal conductivity of monolayer AlN under bi-axial strain: A first principles study, *Physical Chemistry Chemical Physics* [10.1039/D2CP01513G](https://doi.org/10.1039/D2CP01513G) (2022).
- [70] X. Gu and R. Yang, First-principles prediction of phononic thermal conductivity of silicene: A comparison with graphene, *Journal of Applied Physics* **117**, 025102 (2015).
- [71] P. Ying, NEP potential training and testing files for phosphorene, [10.5281/zenodo.6575727](https://doi.org/10.5281/zenodo.6575727) (2022).